N-(4-Hydroxyphenyl)retinamide suppresses SARS-CoV-2 spike protein-mediated cell-cell fusion and viral infection *in vitro*

Yasuhiro Hayashi

    Teikyo University

Kiyoto Tsuchiya

    National Center for Global Health and Medicine Hospital

Mizuki Yamamoto

    The University of Tokyo

Yoko Nemoto-Sasaki

    Teikyo University

Kazunari Tanigawa

    Teikyo University

Kotaro Hama

    Teikyo University

Takashi Tanikawa

    Josai University

Jin Gohda

    The University of Tokyo

Kenji Maeda

    National Center for Global Health and Medicine Research Institute

Jun-ichiro Inoue

    The University of Tokyo

Atsushi Yamashita

    Teikyo University

Research Article

Keywords: SARS-CoV-2, sphingolipid

Abstract

The coronavirus disease (COVID-19) pandemic, caused by severe acute respiratory syndrome coronavirus 2 (SARS-CoV-2), persists worldwide with limited therapeutic options. Since membrane fusion between SARS-CoV-2 and host cells is essential for the early step of the infection, the membrane compositions, including sphingolipids, in host cells are considered to affect the viral infection. However, the role of sphingolipids in the life cycle of SARS-CoV-2 remains unclear. Here, we assessed several inhibitors of sphingolipid metabolism enzymes against SARS-CoV-2 spike protein-mediated cell-cell fusion and viral infection *in vitro*. Among the compounds tested, only *N*-(4-hydroxyphenyl)retinamide (4-HPR, also known as fenretinide), an inhibitor of dihydroceramide Δ4-desaturase 1 (DES1) and well known for having antitumour activity, suppressed cell-cell fusion (50% effective concentration [EC_{50}] = 4.1 mM) and viral infection ([EC_{50}] = 4.4 mM), wherein the EC_{50} values are below its plasma concentration in previous clinical trials on tumours. DES1 catalyses the introduction of a double bond in dihydroceramide, and the inhibition efficiencies observed were consistent with an increased ratio of saturated sphinganine-based lipids to total sphingolipids and the decreased cellular membrane fluidity. These findings, together with the accumulated clinical data regarding the safety of 4-HPR, make it a likely candidate drug to treat COVID-19.

Introduction

The coronavirus disease (COVID-19) pandemic, caused by severe acute respiratory syndrome coronavirus 2 (SARS-CoV-2), originates from Wuhan, Hubei Province, China[1-4]. By the end of December 2020, more than 81 million people have been infected worldwide, with more than 1.7 million deaths in 220 countries (Worldometer website, https://www.worldometers.info/coronavirus/). Although the pandemic wave of COVID-19 continues, therapeutic options remain limited.

Sphingolipids are critical to all stages of the viral life cycle, including the binding of human rhinovirus[5], entry of influenza virus[6], replication of hepatitis C virus[7], and new particle budding of adenovirus[8]. We found that sphingomyelin synthase 2, involved in the synthesis of sphingomyelin (SM), can promote HIV-1 envelope-mediated membrane fusion[9]. Recently, Vitner et al.[10] reported that the glucosylceramide synthase (GCS) inhibitors Genz-123346 and Genz-667161 block the infection of RNA viruses, including neuroinvasive Sindbis virus, West Nile virus, influenza A virus, and SARS-CoV-2. This study suggested that sphingolipids are involved in SARS-CoV-2 infection; however, lipid profiles of inhibitor-treated cells have not yet been examined. Thus, the precise function of sphingolipids in SARS-CoV-2 infection remains unclear.

Sphingolipid metabolism involves a dynamic network of molecules, including important bioactive signalling molecules (Fig. 1)[11,12]. *De novo* biosynthesis of sphingolipids occurs in the endoplasmic reticulum and begins with the condensation of L-serine with palmitoyl-CoA to produce 3-ketodihydrosphingosine in a reaction catalysed by serine palmitoyltransferase (SPT). 3-Ketodihydrosphingosine is reduced to dihydrosphingosine, which is *N*-acylated to dihydroceramide

(DHCer) by ceramide synthase (CerS). The *N*-acyl chain length of DHCer is determined by the specificity of different CerSs; C16:0, C18:0, C24:0, and C24:1 are the major fatty acids incorporated into DHCer in mammalian cells[13]. The formation of ceramide (Cer), the core structure of sphingolipids, involves insertion of a single double bond into DHCer by dihydroceramide Δ4-desaturase 1 (DES1). Cer, and to a lesser extent DHCer, is further metabolised to form complex sphingolipids, such as sphingomyelins (SM and DHSM, respectively) and glucosylceramides (GlcCer and DHGlcCer, respectively) in the Golgi apparatus. Thus, DHCer, DHSM, and DHGlcCer are composed of saturated sphingoid base backbones (sphinganine), while Cer, SM, and GlcCer are composed of unsaturated sphingoid base backbones (sphingosine: Sph). Most of the genes encoding sphingolipid-metabolizing enzymes, as well as several inhibitors of sphingolipid-metabolizing enzymes, have been identified[14-24].

SARS-Cov-2 needs to penetrate the cell membrane in order to infect cells. Therefore, in the present study, we tested a compound, *N*-(4-hydroxyphenyl)retinamide (4-HPR, also known as fenretinide), which would change the membrane environment in such a way that makes virus penetration difficult, thereby preventing infection. We found that 4-HPR could prevent viral entry into host cells, due to decreased membrane fluidity. Furthermore, to understand the function of sphingolipids in SARS-CoV-2 infection, we analysed the quantitative sphingolipid metabolome of inhibitor-treated cells using liquid chromatography-tandem mass spectrometry (LC-MS/MS). We found that the quality of the sphingoid base backbone (saturated or unsaturated), and not the total quantity of sphingolipids, is involved in SARS-CoV-2 infection.

Results

4-HPR inhibits SARS-CoV-2 spike (S) protein-mediated cell-cell fusion

Since membrane fusion between SARS-CoV-2 and host cells is essential for the early step of the infection, the membrane compositions, including sphingolipids, in host cells are considered to affect the viral infection. To investigate the roles of sphingolipids in SARS-CoV-2 S protein-meditated membrane fusion, we employed the dual split protein (DSP)-based cell-cell fusion assay using SARS-CoV-2 mimicking cells and sphingolipid-manipulated target cells treated with an inhibitor of sphingolipid metabolism enzyme. The membrane fusion efficiency between 293FT/SARS-CoV-2 S/DSP8-11 cells, as effector cells (HEK293FT cells stably expressing SARS-CoV-2 S protein and DSP8–11), and 293FT/ACE2/TMPRSS2/DSP1-7 cells, as target cells (HEK293FT cells stably expressing SARS-CoV-2 receptor angiotensin-converting enzyme 2: ACE2, transmembrane serine protease 2: TMPRSS2, and DSP1–7), can be monitored by measuring the activity of *Renilla* luciferase (RL) because of DSP1-7 and DSP8-11 reassociation[25] (Fig. 2a). We assessed 13 compounds, including 12 inhibitors of sphingolipid metabolism enzymes and an inactive stereoisomer of *threo*-PPMP (an inhibitor of GCS), against SARS-CoV-2 S protein-meditated membrane fusion. Before evaluating the activity of compounds against cell-cell fusion, a nontoxic concentration of each compound for the cells was determined using a WST-8 assay, allowing the determination of the number of viable cells by a sensitive colorimetric method. When 293FT/ACE2/TMPRSS2/DSP1-7 cells were exposed to various concentrations of compounds for 2 days,

no effect on cell viability was observed for myriocin, fumonicin B1, conduritol B epoxide (CBE), HPA12, and amitriptyline at concentrations above 40 mM (Fig. 2b). While, GT11, threo-PPMP, erythro-PPMP, GW4869, and SKI-II exhibited cytotoxicity above 20 mM, 4-HPR and FTY720 exhibited cytotoxicity above 10 mM, and ceranib-2 showed cytotoxicity above 2.5 mM.

We next assessed the effects of the 13 compounds against the SARS-CoV-2 S protein-mediated cell-cell fusion at nontoxic concentrations of each compound (Fig. 2c). The analysis of cell-cell fusion revealed that 4-HPR, threo-PPMP, and erythro-PPMP inhibited DSP activity by more than 50% compared with that of the solvent-only control containing dimethyl sulfoxide (DMSO). Importantly, luciferase activity derived from cells carrying the preformed DSP1-7/DSP8-11 reporter complex was not affected by 4-HPR, threo-PPMP, and erythro-PPMP (Supplementary Fig. 1a), indicating that the suppression of luciferase activity reflects the inhibition of cell-cell fusion by these compounds. However, little or no anti-membrane fusion activity was found for myriocin, fumonicin B1, GT11, CBE, HPA12, GW4869, amitriptyline, ceranib-2, SKI-II, and FTY720.

To investigate changes in sphingolipid levels in inhibitor-treated cells, we next quantified sphingolipids using LC-MS/MS. Importantly, the levels of all species with a distinct acyl chain in DHCer, DHGlcCer, and DHSM (panels g-l in Supplementary Figs. 2, 3, and 4) and total levels of DHCer, DHGlcCer, and DHSM (lower panels in Fig. 3a–c) increased in 5 mM 4-HPR-treated cells compared with that in 10 mM GT11-treated cells. This observation was despite the fact that both compounds inhibit the same enzyme, DES1. The ratio of saturated sphinganine-based lipids to total sphingolipids was close to 20% in 5 mM 4-HPR-treated cells, but 10% for 2.5 mM 4-HPR or 10 mM GT11 treatments (Fig. 3e). We found that the increased ratio was consistent with the inhibition efficiencies of cell-cell fusion (Fig. 2c and Fig. 3e).

As expected, treatment with myriocin and fumonicin B1, inhibitors of de novo sphingolipid biosynthesis, significantly decreased the levels of most species with a distinct acyl chain in Cer, GlcCer, and SM (panels a-f in Supplementary Figs. 2, 3, and 4), and total levels of Cer, GlcCer, and SM (upper panels in Fig. 3a-c) compared with that for DMSO treatment. As a result, cells treated with myriocin and fumonicin B1 showed a reduction of approximately 65% and 79% in total sphingolipid levels, respectively (Fig. 3d). These changes had little effect on SARS-CoV-2 S protein-mediated cell-cell fusion, indicating that the total quantity of sphingolipid was not involved.

Contrary to the expectations, cells treated with 10 mM erythro-PPMP, an inactive stereoisomer of GCS inhibitor threo-PPMP, exhibited a decreased level of GlcCer compared with that in DMSO-treated cells, although to a lesser extent than that in cells treated with threo-PPMP (upper panel in Fig. 3b). Given that myriocin and fumonicin B1 reduced the levels of all GlcCer species as much as, or more than that by threo-PPMP (panels a-f in Supplementary Fig. 3), no correlation was observed between the GlcCer levels and inhibition efficiency against cell-cell fusion. Thus, the inhibition of cell-cell fusion caused by 10 mM threo-PPMP and 10 mM erythro-PPMP might be potential off-target effects.

4-HPR inhibits SARS-CoV-2 infection *in vitro*

We further examined antiviral activity of three compounds 4-HPR, *threo*-PPMP, and *erythro*-PPMP, which inhibited SARS-CoV-2 S protein-mediated cell-cell fusion by more than 50%. In addition to these compounds, myriocin and GT11 were also used to investigate the function of sphingolipids in viral infection. When VeroE6^{TMPRSS2} cells were exposed to various concentrations of the compounds for 3 days, myriocin, at a concentration above 20 mM, exhibited no effect on cell viability (Fig. 4a). In contrast, *threo*-PPMP and *erythro*-PPMP exhibited cytotoxicity at concentrations above 20 mM, while 4-HPR and GT11 showed cytotoxicity above 10 mM.

We next assessed the effects of the compounds against SARS-CoV-2 infection at nontoxic concentrations (Fig. 4b). Note that 4-HPR, and not GT11, was found to have potent antiviral activity against SARS-CoV-2 NCGM-05-2N strain (SARS-CoV-2^{05-2N}) with a 50% effective concentration (EC$_{50}$) value of 4.4 mM. Cells treated with 5 mM and 2.5 mM 4-HPR inhibited viral infection by about 60% and 15%, respectively. However, no antiviral activity was observed at concentrations lesser than 1.3 mM 4-HPR, 5 mM GT11, 10 mM *threo*-PPMP, or 10 mM *erythro*-PPMP.

The analysis of sphingolipid levels with LC-MS/MS revealed that the ratio of saturated sphinganine-based lipids to total sphingolipids in 4-HPR-treated cells increased in a concentration-dependent manner, exhibiting 25% inhibition for 5 mM 4-HPR, 17% for 2.5 mM 4-HPR, and 12% for 1.3 mM 4-HPR treatment (Fig. 4c). Furthermore, no significant difference in the ratio of saturated sphinganine-based lipids to total sphingolipids was observed between 1.3 mM 4-HPR and 5 mM GT11 treatments (Fig. 4c). These results were consistent with the inhibition efficiencies of viral infection (Fig. 4b). Thus, the quality of the sphingoid base backbone, saturated or unsaturated, was found to be involved in SARS-CoV-2 infection.

In contrast, myriocin, *threo*-PPMP, and *erythro*-PPMP were not found to exhibit antiviral activity (Fig. 4b). The cells treated with myriocin showed approximately 50% reduction in total sphingolipid levels (Fig. 4d), and those with *threo*-PPMP showed approximately 60% reduction in total GlcCer levels (upper panel in Supplementary Fig. 5b) compared with that by treatment with DMSO. These results indicated that the total quantity of sphingolipids, including GlcCer, was not involved in SARS-CoV-2 infection.

4-HPR-treated cells display decreases in membrane fluidity

Finally, we examined the cellular effect of 4-HPR to obtain mechanistic insight into the inhibitory effect of 4-HPR on SARS-CoV-2 S protein-mediated cell-cell fusion and viral infection. Because cell-cell fusion and viral infection were considered to be strictly dependent on the cell-surface levels of the SARS-CoV-2 receptor ACE2, we examined the effect of 4-HPR on the expression of ACE2 in 293FT/ACE2/TMPRSS2/DSP1-7 cells and VeroE6^{TMPRSS2} cells. Importantly, no significant differences were observed in the ACE2 expression levels in the 293FT/ACE2/TMPRSS2/DSP1-7 cells treated with 5 mM 4-HPR compared with that in the cells treated with DMSO or 10 mM GT11 (Fig. 5a). Similar results

were obtained with VeroE6[TMPRSS2] cells (Supplementary Fig. 9a). These results indicated that the inhibition of cell-cell fusion and viral infection by 4-HPR was not attributable to the ACE2 expression levels on the cell surface.

Lipid rafts are defined as detergent-resistant sphingolipid-rich microdomains of cellular membranes[26]. Several viral receptors are known to be localised in the lipid rafts and are involved in efficient viral infection[27, 28]. We next examined whether 4-HPR treatment affected the localization of ACE2 on the membrane microdomain. When we treated 293FT/ACE2/TMPRSS2/DSP1-7 cells with the non-ionic detergent TritonX-100, ACE2 was found in the detergent-solubilised membrane fraction in which the non-raft marker transferrin receptor protein was localised, but not flotillin, the raft marker protein (Fig. 5b). Furthermore, ACE2 did not redistribute to the lipid raft domains even in the presence of SARS-CoV-2 S protein stimulation (Fig. 5b). Importantly, we observed no dramatic difference in ACE2 localization in the membrane microdomain between the DMSO and 4-HPR treatments (Fig. 5b), indicating that the inhibition of cell fusion by 4-HPR was not attributable to ACE2 localization on the membrane microdomain.

Lipid saturation is known to be important for membrane fluidity[29]. In addition, it has been demonstrated that an increase in DHSM is associated with the rigidification of the cell membrane, which can inhibit HIV-1 infection[30]. We therefore examined the effect of 4-HPR on cellular membrane fluidity using lipophilic pyrene probes, which undergo excimer formation with increasing membrane fluidity[31]. Cells treated with 5 mM and 2.5 mM 4-HPR exhibited decreased membrane fluidity by about 50% and 20%, respectively, compared with that in cells treated with DMSO (Fig. 5c). In addition, membrane fluidity was not significantly different between the cells treated with 2.5 mM 4-HPR and 10 mM GT11. Importantly, these results were consistent with the inhibition efficiencies of SARS-CoV-2 S protein-mediated cell-cell fusion (Fig. 2c) and the increased ratio of saturated sphinganine-based lipids to total sphingolipids (Fig. 3e). Similar results were obtained with VeroE6[TMPRSS2] cells (Supplementary Fig. 9b). These findings suggested that a decrease in cellular membrane fluidity by 4-HPR might be a major cause of the inhibition of SARS-CoV-2 S protein-mediated cell-cell fusion and viral infection.

Discussion

In this study, we clearly showed that 4-HPR could prevent SARS-CoV-2 entry into cells due to a decrease in membrane fluidity, and not the location of the ACE2 receptor within the membrane compartments. Furthermore, we found that the quality of the sphingoid base backbone, and not the total quantity of sphingolipids, was involved in SARS-CoV-2 infection.

Interestingly, no significant activity against cell-cell fusion or viral infection was found for myriocin, although the total sphingolipid levels significantly decreased in the myriocin-treated cells compared with that in the DMSO-treated cells. Lipid rafts, sphingolipid-enriched microdomains in cellular membranes, were not a major localization site for ACE2 in 293FT/ACE2/TMPRSS2/DSP1-7 cells. This might explain why the quantity of sphingolipids did not appear to be involved in SARS-CoV-2 infection. We observed no clear localization of ACE2 in VeroE6[TMPRSS2] cells, as determined biochemically using TritonX-100

solubilization, since the expression level of ACE2 in these cells was lower than in 293FT/ACE2/TMPRSS2/DSP1-7 cells (data not shown). It has been reported that ACE2 is localised within non-raft domains in Chinese hamster ovary cells[32] and VeroE6 cells[33], whereas other groups have reported ACE2 localization within raft domains in VeroE6 cells[34, 35]. Although the cause of discrepancies between these findings is unknown, importantly, in this study ACE2 did not redistribute to the lipid raft domains even in the presence of SARS-CoV-2 S protein stimulation. Given that, we propose that ACE2 localization on the membrane microdomain is not essential for SARS-CoV-2 entry into host cells at least in our infection study.

We found that the increased ratio of saturated sphinganine-based lipids (DHCer, DHGlcCer, and DHSM) to total sphingolipids was correlated with the inhibition efficiencies of cell-cell fusion and viral infection. The antiviral activity of 4-HPR has been proved in different viruses[36-39]; however, the mechanism of inhibition remains unclear. Finnegan et al.[36] reported that 4-HPR increases cellular Cer, and not DHCer, levels, which is thought to be a cause of inhibition of HIV-1 infection. More specifically, at that time it was thought that 4-HPR elevates Cer levels, but not DHCer, by activation of SPT and CerS[40, 41]. However, it was later revealed that the increased lipid level is due to DHCer rather than Cer; DHCer accumulation is caused by 4-HPR inhibition of DES1[42]. Therefore, here, we first clarified the relationship between the accumulation of saturated sphinganine-based lipids by 4-HPR and suppression of viral infection. Among the saturated sphinganine-based lipids in 293FT/ACE2/TMPRSS2/DSP1-7 cells treated with 4-HPR, DHSM constituted 65%, DHCer 34.5%, and DHGlcCer 0.5% (data not shown). Further research is needed to elucidate the role of each lipid involved in infection, which will aid in establishing the functions of saturated sphinganine-based lipids against SARS-CoV-2 infection.

Treatment with 4-HPR increased the ratio of saturated sphinganine-based lipids to total sphingolipids more than that by treatment with GT11 in 293FT/ACE2/TMPRSS2/DSP1-7 cells and VeroE6[TMPRSS2] cells, although GT11 competitively inhibits DES1 activity in rat liver microsomes higher than 4-HPR (IC_{50} of GT11 = 0.69 mM; IC_{50} of 4-HPR= 2.32 mM)[43]. It is also known that 4-HPR increases the levels of reactive oxygen species intracellularly[44], and DES1 activity is inhibited by oxidative stress[45]. Casasampere et al.[12] suggested that 4-HPR inhibition of DES1 may occur indirectly through increased oxidative species. Therefore, both direct and indirect inhibitory effects of 4-HPR on DES1 might have effectively increased the ratio of saturated sphinganine-based lipids to total sphingolipids more than that by GT11.

Our findings clearly indicated that 4-HPR potently inhibited SARS-CoV-2 S protein-mediated membrane fusion in a cell-cell fusion assay system (EC_{50} = 4.1 mM) and viral infection *in vitro* (EC_{50} = 4.4 mM). 4-HPR is a synthetic derivative of all-*trans*-retinoic acid, which has been widely investigated for the treatment of cancer[46-49]. In a phase I study of 4-HPR oral powder administered to patients with relapsed/refractory neuroblastoma, the day 6 mean peak plasma concentration has been noted as 21 mM 4-HPR at a dose of 1500 mg/m^2 per day[46]. Given that the EC_{50} value for 4-HPR against SARS-CoV-2 infection was below its plasma concentration (4.4 mM vs. of 21 mM) in this study, 4-HPR might serve as a potential therapeutic agent for COVID-19, as predicted by another group[50]. Furthermore, a low-toxicity

profile of 4-HPR has been observed in many clinical trials, as well as in long-term treatments[46-49]. Therefore, the findings of this study, together with the accumulated clinical data regarding the safety of 4-HPR, make it a likely candidate drug to treat COVID-19. Furthermore, 4-HPR could be a potential preventative therapy against SARS-CoV-2 infection, which unlike the vaccines could be administered via an inhaler or a spray to the airways, perhaps by self-administration, thereby relieving the pressure on the healthcare system. Nonetheless, further studies using animal models, such as ferrets, are needed to clarify the role of 4-HPR in SARS-CoV-2 infection *in vivo*.

Methods

Cells and viruses

HEK293FT cells expressing the SARS-CoV-2 S protein and DSP8-11 (293FT/SARS-CoV-2 S/DSP8-11) were maintained in D-MEM supplemented with 10% foetal calf serum (FCS), 100 mg/mL penicillin, 100 mg/mL streptomycin, 1 mg/mL puromycin, and 10 mg/mL blasticidin. HEK293FT cells expressing ACE2, TMPRSS2, and DSP1-7 (293FT/ACE2/TMPRSS2/DSP1-7) were maintained in D-MEM supplemented with 10% FCS, 100 mg/mL penicillin, 100 mg/mL streptomycin, 1 mg/mL puromycin, 10 mg/mL blasticidin, and 300 mg/mL hygromycin. HEK293FT cells expressing DSP8-11 (293FT/DSP8-11) were maintained in D-MEM supplemented with 10% FCS, 100 µg/mL penicillin, 100 µg/mL streptomycin, and 1 mg/mL puromycin. VeroE6^{TMPRSS2} cells were obtained from the Japanese Collection of Research Bioresources Cell Bank (Osaka, Japan)[51]. VeroE6^{TMPRSS2} cells were maintained in D-MEM supplemented with 10% FCS, 100 µg/mL of penicillin, 100 µg/mL of streptomycin, and 1 mg/mL of geneticin antibiotic. SARS-CoV-2 NCGM-05-2N strain (SARS-CoV-2^{05-2N}) was isolated from nasopharyngeal swabs of a patient with COVID-19 who was admitted to the National Center for Global Health and Medicine, Tokyo, Japan.

Chemicals and antibodies

Myriocin, SKI-II, and FTY720 were obtained from Abcam (Cambridge, UK). Fumonicin B1, CBE, amitriptyline, and ceranib-2 were obtained from Sigma-Aldrich (St. Louis, MO, USA). 4-HPR and HPA12 were obtained from Tokyo Chemical Industry (Tokyo, Japan). GT11 was obtained from Avanti Polar Lipids (Alabaster, AL, USA). DL-*threo*-PPMP, DL-*erythro*-PPMP, and GW4869 were obtained from Cayman Chemical (Ann Arbor, MI, USA). All compounds were dissolved in DMSO and diluted to a final concentration of 0.2% DMSO in cell culture medium.

Mouse IgG1 monoclonal anti-ACE2 antibody (catalogue no. 66699-1-Ig) was obtained from Proteintech Group Inc. (Rosemont, IL, USA). Mouse IgG1 isotype control was obtained from BioLegend (San Diego, CA, USA). Goat PE-conjugated anti-mouse IgG polyclonal antibody (catalogue no. 12-4010-82) was obtained from Thermo Fisher Scientific (Waltham, MA, USA). *N*-palmitoyl-d31-*D*-erythro-sphingosine (D31-Cer) and *N*-palmitoyl-d31-*D*-erythro-sphingosylphosphorylcholine (D31-SM) were obtained from Avanti

Polar Lipids, and *N*-omega-d3-hexadecanoyl-glucopsychosine (D3-GlcCer) was obtained from Cayman Chemical.

Rabbit polyclonal anti-ACE2 antibody (catalogue no. ab15348), rabbit IgG monoclonal anti-transferrin receptor antibody (catalogue no. ab214039), and rabbit IgG monoclonal anti-flotillin 1 antibody (catalogue no. ab133497) were obtained from Abcam. Goat horseradish peroxidase-conjugated anti-rabbit IgG antibody (catalogue no. 7074S) was obtained from Cell Signaling Technology (Beverly, MA, USA).

Cytotoxicity assay

293FT/ACE2/TMPRSS2/DSP1-7 and VeroE6^{TMPRSS2} cells were seeded in 96-well plates at 1×10^4 cells/well and 5×10^3 cells/well, respectively. On the following day, the cells were cultured with the specific compounds for 2 days (293FT/ACE2/TMPRSS2/DSP1-7 cells) or 3 days (VeroE6^{TMPRSS2} cells), and then the 50% cytotoxic concentration (CC$_{50}$) values were determined using the WST-8 assay employing Cell Counting Kit-8 (Dojindo, Kumamoto, Japan).

DSP-based cell-cell fusion assay

The cell-cell fusion assay was conducted as previously described by Yamamoto et al.[25], with slight modifications. Target cells (293FT/ACE2/TMPRSS2/DSP1-7) and effector cells (293FT/SARS-CoV-2 S/DSP8-11) were seeded in 24-well plates at 4×10^4 cells/well. On the following day, the medium of the target cells was exchanged with D-MEM containing 10% FCS and various concentrations of each of the compounds to be tested, and the cells were incubated for an additional 2 days. Cells were washed with phosphate-buffered saline (PBS) and were detached using Cellstripper containing EDTA but no trypsin (Corning, Christiansburg, VA, USA). Cells were resuspended in serum-free D-MEM and centrifuged at 500 × *g* for 2 min. After aspirating the suspension, cells were resuspended in serum-free D-MEM containing 1% Nutridoma SP (Roche, Basel, Switzerland) and 6 mM EnduRen (Promega, Madison, WI, USA), a substrate for RL. The effector and target cells were mixed in the wells of a 96-well plate, and after incubating at 37 °C for 4 h the RL activity was measured using a SpectraMax i3x Microplate Reader (Molecular Devices, San Jose, CA, USA).

Antiviral assay

VeroE6^{TMPRSS2} cells were seeded in 96-well plates (5×10^3 cells/well). On the following day, the cells were cultured with each of the tested compounds for 3 days before adding SARS-CoV-2^{05-2N}. The cells were inoculated at a multiplicity of infection of 0.01. After culturing the cells with the specific compounds and

SARS-CoV-2[05-2N] for 3 days, the level of cytopathic effect observed in SARS-CoV-2-exposed cells was determined using the WST-8 assay.

Lipid extraction and quantification of sphingolipids by LC-MS/MS

Lipid extraction and quantification of sphingolipids by LC-MS/MS were performed as described previously[52-54]. 293FT/ACE2/TMPRSS2/DSP1-7 and VeroE6[TMPRSS2] cells were seeded in 6-well plates at 2×10^5 cells/well and 7×10^4 cells/well, respectively. On the following day, the cells were cultured with each of the tested compounds for 2 days (293FT/ACE2/TMPRSS2/DSP1-7 cells) or 3 days (VeroE6[TMPRSS2] cells), after which the cells were washed once with cold PBS, collected in 100 mL of cold PBS, and then homogenised by sonication. Part of the sample (5 mL) was used in the bicinchoninic acid protein assay to determine the amount of protein. Total lipids were extracted by adding 375 mL of chloroform:methanol (1:2, v/v) containing 40 pmol of each component, specifically D31-Cer, D31-SM, and D3-GlcCer. Deuterated D31-Cer, D31-SM, and D3-GlcCer were used as internal standards for Cer and DHCer, SM and DHSM, and GlcCer and DHGlcCer, respectively. After sonicating the single-phase mixture, 100 mL of chloroform:methanol:5N NaOH (1:2:0.8, v/v/v) was added and the solution was incubated for 1 h at 37 °C, followed by neutralisation with acetic acid. Subsequently, 158 mL of chloroform and 158 mL of water were added and the mixture was then vigorously shaken using a vortex, before centrifuging for 1 min at 13,000 × g at 4 °C. The lower phase was withdrawn and dried and then resuspended in acetonitrile:methanol (1:1, v/v), sonicated for 10 s, centrifuged at 14,000 × g for 5 min, and the supernatant was transferred to vials. The concentrations of Cer, DHCer, GlcCer, DHGlcCer, SM, and DHSM were analysed using the QTRAP4500 instrument (SCIEX, Framingham, MA, USA). Sphingolipids containing C16:0, C18:0, C20:0, C22:0, C24:0, and C24:1 fatty acids were detected using a multiple reaction monitoring method, as described in Supplementary Table 1.

Analysis of cell-surface expression of ACE2

293FT/ACE2/TMPRSS2/DSP1-7 cells in 24-well plates were treated with the indicated concentrations of the compounds for 2 days. Cells were harvested by Cellstripper (Corning) and fixed with 4% formaldehyde before incubation with either anti-ACE2 antibody (Proteintech) or mouse IgG1 isotype control (BioLegend) antibody at 4 °C. Cells were then stained with PE-conjugated secondary antibody (Thermo Fisher Scientific) and analysed using the FACSCanto II instrument (BD Biosciences, San Jose, CA, USA). Data were analysed with FlowJo software (Tree Star Inc., San Carlos, CA, USA).

S protein stimulation of 293FT/SARS-CoV-2 S/DSP8-11 cells and isolation of lipid raft domains

Target cells (293FT/ACE2/TMPRSS2/DSP1-7), S protein expressing cells (293FT/SARS-CoV-2 S/DSP8-11), and cells not expressing S protein (293FT/DSP8-11) were seeded at 7×10^5 cells per 10-cm-diameter dish. On the following day, the medium of the target cells was exchanged with D-MEM containing 10% FCS and 5 mM 4-HPR, and the cells were incubated for an additional 2 days. Cells were then washed with PBS and detached by Cellstripper (Corning) before resuspending in serum free D-MEM and centrifuging at $500 \times g$ for 2 min. After aspirating the suspension, the cells were resuspended in serum-free D-MEM containing 1% Nutridoma SP (Roche). The target cells were mixed with 293FT/SARS-CoV-2 S/DSP8-11 (presence of SARS-CoV-2 S protein stimulation) or 293FT/DSP8-11 (absence of SARS-CoV-2 S protein stimulation) cells, incubated for 30 min, and then washed with cold PBS. Subsequently, sucrose gradient analysis for ACE2 was performed as described previously[55] with slight modifications. The pellets were homogenised in 2 mL of TNE buffer (25 mM Tris-HCl, pH 7.5, 150 mM NaCl, and 1 mM EDTA) with 0.1% TritonX-100. The sucrose content of the homogenate was then adjusted to 40% by adding 80% sucrose. A linear sucrose gradient (5–30%) in 7 mL of TNE buffer without TritonX-100 was layered over the lysate. The gradients were centrifuged for 17 h at $200,000 \times g$ at 4 °C using a P40ST rotor (Hitachi Koki Co., Ltd, Tokyo, Japan). Eleven fractions were collected from the top of the gradient, followed by immunoblot analysis using anti-ACE2, anti-transferrin receptor (non-raft marker), and anti-flotillin 1 (raft marker) antibodies (all from Abcam).

Analysis of cellular membrane fluidity

Analysis of membrane fluidity was performed as described previously[56] with slight modifications. Briefly, 293FT/ACE2/TMPRSS2/DSP1-7 cells in 24-well plates were treated with the indicated concentrations of the compounds for 2 days. Cells were detached by Cellstripper (Corning), resuspended in PBS, and centrifuged at $500 \times g$ for 2 min. The suspension was aspirated and the cells were labelled with a solution of 15 mM pyrenedecanoic acid and 0.08% F-127 in perfusion buffer, in the dark for 20 min with rocking at 25 °C. Excess probe was removed and the cells were washed with PBS. The cells were resuspended in 450 mL PBS; 200 mL was aliquoted into a 96-well plate and fluorescence was measured using an excitation wavelength of 350 nm and two emission wavelengths: 400 nm for the monomer and 470 nm for the excimer, using a SpectraMax i3x Microplate reader (Molecular Devices). The ratio of excimer to monomer fluorescence is related to cellular membrane fluidity, with a higher ratio reflecting greater fluidity.

Statistical analysis

All statistical analyses were performed with GraphPad PRISM 6 (GraphPad Software, San Diego, CA, USA).

Data availability

Data that support the findings of this study are available from the corresponding author upon reasonable requests. Source data are provided within this paper.

References

1. Zhu, N., et al. A novel coronavirus from patients with pneumonia in China, 2019. *New Engl. J. Med.* **382**, 727-733 (2020).

2. Zhou, P., et al. A pneumonia outbreak associated with a new coronavirus of probable bat origin. *Nature* **579**, 270-273 (2020).

3. Li, Q., et al. Early transmission dynamics in Wuhan, China, of novel coronavirus-infected pneumonia. *New Engl. J. Med.* **382**, 1199-1207 (2020).

4. Mitsuya, H. & Kokudo, N. Sustaining containment of COVID-19: global sharing for pandemic response. *Health Med.* **2**, 53-55 (2020).

5. Grassmé, H., Riehle, A., Wilker, B., & Gulbins, E. Rhinoviruses infect human epithelial cells via ceramide-enriched membrane platforms. *Biol. Chem.* **280**, 26256-26262 (2005).

6. Drews, K., et al. Glucosylceramide synthase maintains influenza virus entry and infection. *PloS one* **15**, e0228735 (2020).

7. Weng, L., et al. Sphingomyelin activates hepatitis C virus RNA polymerase in a genotype-specific manner. *Virol.* **84**, 11761-11770 (2010).

8. Kanj, S.S., et al. Ceramide regulates SR protein phosphorylation during adenoviral infection. *Virology* **345**, 280-289 (2006).

9. Hayashi, Y., et al. Sphingomyelin synthase 2, but not sphingomyelin synthase 1, is involved in HIV-1 envelope-mediated membrane fusion. *Biol. Chem.* **289**, 30842-30856 (2014).

10. Vitner, E.B., et al. Antiviral activity of glucosylceramide synthase inhibitors against SARS-CoV-2 and other RNA virus infections. bioRxiv https://doi.org/10.1101/2020.05.18.103283 (2020).

11. Bartke, N. & Hannun, Y.A. Bioactive sphingolipids: metabolism and function. *Lipid Res.* **50**, 91-96 (2009).

12. Casasampere, M., Ordoñnez, Y. F., Pou, A., & Casas, J. Inhibitors of dihydroceramide desaturase 1: Therapeutic agents and pharmacological tools to decipher the role of dihydroceramides in cell biology. *Phys. Lipids* **197**, 33-44 (2016).

13. Shaner, R.L., et al. Quantitative analysis of sphingolipids for lipidomics using triple quadrupole and quadrupole linear ion trap mass spectrometers. *Lipid Res.* **50**, 1692-1707 (2009).

14. Miyake, Y. et al. Serine palmitoyltransferase is the primary target of a sphingosine-like immunosuppressant, ISP-1/myriocin. *Biophys. Res. Commun.* **211**, 396-403 (1995).

15. Merrill, A.H., van Echten, G., Wang, E., & Sandhoff, K. Fumonisin B1 inhibits sphingosine (sphinganine) *N*-acyltransferase and de novo sphingolipid biosynthesis in cultured neurons *in situ*.

Biol. Chem. **268**, 27299-27306 (1993).

16. Triola, G., Fabriàs, G., & Llebaria, A. Synthesis of a cyclopropene analogue of ceramide, a potent inhibitor of dihydroceramide desaturase. *Chem. Int. Ed.* **40**, 1960-1962 (2001).

17. Wang, H., et al. N-(4-Hydroxyphenyl)retinamide increases dihydroceramide and synergizes with dimethylsphingosine to enhance cancer cell killing. *Cancer Ther.* **7**, 2967-2976 (2008).

18. Yasuda, S., et al. A novel inhibitor of ceramide trafficking from the endoplasmic reticulum to the site of sphingomyelin synthesis. *Biol. Chem.* **276**, 43994-44002 (2001).

19. Abe, A., *et al.* Improved inhibitors of glucosylceramide synthase. *Biochem.* **111**, 191-196 (1992).

20. Luberto, C., et al. Inhibition of tumor necrosis factor-induced cell death in MCF7 by a novel inhibitor of neutral sphingomyelinase. *Biol. Chem.* **277**, 41128-41139 (2002).

21. Elojeimy, S., et al. New insights on the use of desipramine as an inhibitor for acid ceramidase. *FEBS Lett.* **580**, 4751-4756 (2006).

22. Draper, J.M., et al. Discovery and evaluation of inhibitors of human ceramidase. *Cancer Ther.* **10**, 2052-2061 (2011).

23. French, K.J., et al. Discovery and evaluation of inhibitors of human sphingosine kinase. *Cancer Res.* **63**, 5962-5969 (2003).

24. Brinkmann, V., et al. The immune modulator FTY720 targets sphingosine 1-phosphate receptors. *Biol. Chem.* **277**, 21453-21457 (2002).

25. Yamamoto, M., et al. The anticoagulant nafamostat potently inhibits SARS-CoV-2 S protein-mediated fusion in a cell fusion assay system and viral infection in vitro in a cell-type-dependent manner. *Viruses* **12**, https://doi.org/10.3390/v12060629 (2020).

26. Brown, D.A. & Rose, J.K. Sorting of GPI-anchored proteins to glycolipid-enriched membrane subdomains during transport to the apical cell surface. *Cell* **68**, 533-544 (1992).

27. Popik, W., Alce, T.M., & Au, W-C. Human immunodeficiency virus type 1 uses lipid raft-colocalized CD4 and chemokine receptors for productive entry into CD4(+) T cells. *Virol.* **76**, 4709-4722 (2002).

28. Takeda, M., Leser, G.P., Russell, C.J. & Lamb, R.A. Influenza virus hemagglutinin concentrates in lipid raft microdomains for efficient viral fusion. *Natl. Acad. Sci. USA* **100**, 14610-14617 (2003).

29. Rodriguez-Cuenca, S., et al. Stearoyl-CoA Desaturase 1 is a key determinant of membrane lipid composition in 3T3-L1 adipocytes. *PLoS One* **11**, e0162047 (2016).

30. Vieira, C.R., et al. Dihydrosphingomyelin impairs HIV-1 infection by rigidifying liquid-ordered membrane domains. *Biol.* **17**, 766-775 (2010).

31. Uddin, M.G. & Azam, Z. A novel oligo-DNA probe carrying non-nucleosidic silylated pyrene derivatives: synthesis and excimer forming ability. *J. Biochem. Mol. Biol.* **3**, 175-181 (2013).

32. Warner, F.J., et al. Angiotensin-converting enzyme 2 (ACE2), but not ACE, is preferentially localized to the apical surface of polarized kidney cells. *Biol. Chem.* **280**, 39353-39362 (2005).

33. Li, G.M., et al. Lipid rafts play an important role in the early stage of severe acute respiratory syndrome-coronavirus life cycle. *Microbes Infect.* **9**, 96-102 (2007).

34. Lu, Y., Liu, D.X., & Tam, J.P. Lipid rafts are involved in SARS-CoV entry into Vero E6 cells. *Biophys. Res. Commun.* **369**, 344-349 (2008).

35. Glende, J., et al. Importance of cholesterol-rich membrane microdomains in the interaction of the S protein of SARS-coronavirus with the cellular receptor angiotensin-converting enzyme 2. *Virology* **381**, 215-221 (2008).

36. Finnegan, C.M., et al. Ceramide, a target for antiretroviral therapy. *Natl. Acad. Sci. USA* **101**, 15452-15457 (2004).

37. Fraser, J.E. et al. A nuclear transport inhibitor that modulates the unfolded protein response and provides in vivo protection against lethal dengue virus infection. *Infect. Dis.* **210**, 1780-1791 (2014).

38. Yan, D., et al. Replication-competent influenza virus and respiratory syncytial virus luciferase reporter strains engineered for co-infections identify antiviral compounds in combination screens. *Biochemistry* **54**, 5589-5604 (2015).

39. Pitts, J.D., Li, P-C., de Wispelaere, M., & Yang, P.L. Antiviral activity of *N*-(4-hydroxyphenyl) retinamide (4-HPR) against Zika virus. *Antiviral Res.* **147**, 124-130 (2017).

40. Maurer, B.J., et al. Synergistic cytotoxicity in solid tumor cell lines between *N*-(4-hydroxyphenyl)retinamide and modulators of ceramide metabolism. *Natl. Cancer Inst.* **92**, 1897-1909 (2000).

41. Morales, M.C., et al. 4-HPR-mediated leukemia cell cytotoxicity is triggered by ceramide-induced mitochondrial oxidative stress and is regulated downstream by Bcl-2. *Free Radic. Res.* **41**, 591-601 (2007).

42. Wang, H., et al. *N*-(4-Hydroxyphenyl)retinamide increases dihydroceramide and synergizes with dimethylsphingosine to enhance cancer cell killing. *Cancer Ther.* **7**, 2967-2976 (2008).

43. Rahmaniyan, M., et al. Identification of dihydroceramide desaturase as a direct in vitro target for fenretinide. *Biol. Chem.* **286**, 24754-24764 (2011).

44. Oridate, N., et al. Involvement of reactive oxygen species in *N*-(4-Hydroxyphenyl)retinamide-induced apoptosis in cervical carcinoma cells. *Natl. Cancer Inst.* **89**, 1191-1198 (1997).

45. Idkowiak-Baldys, J., et al. Dihydroceramide desaturase activity is modulated by oxidative stress. *J.* **427**, 265-274 (2010).

46. Maurer, B.J., et al. Phase I trial of fenretinide delivered orally in a novel organized lipid complex in patients with relapsed/refractory neuroblastoma: a report from the New Approaches to Neuroblastoma Therapy (NANT) consortium. *Blood Cancer* **60**, 1801-1808 (2013).

47. Veronesi, U., et al. Fifteen-year results of a randomized phase III trial of fenretinide to prevent second breast cancer. *Oncol.* **17**, 1065-1071 (2006).

48. Villablanca, J.G., et al. Phase I trial of oral fenretinide in children with high-risk solid tumors: a report from the Children's Oncology Group (CCG 09709). *Clin. Oncol.* **24**, 3423-3430 (2006).

49. Mody, N. & McIlroy, G.D. The mechanisms of Fenretinide-mediated anti-cancer activity and prevention of obesity and type-2 diabetes. *Pharmacol.* **91**, 277-286 (2014).

50. Orienti, I., Gentilomi, G.A. & Farruggia, G. Pulmonary delivery of fenretinide: A possible adjuvant treatment in COVID-19. *J. Mol. Sci.* **21**, https://doi.org/10.3390/ijms21113812 (2020).

51. Matsuyama, S., et al. Enhanced isolation of SARS-CoV-2 by TMPRSS2-expressing cells. *Natl. Acad. Sci. U S A* **117**, 7001-7003 (2020).

52. Bligh, E.G. & Dyer, W.J. A rapid method of total lipid extraction and purification. *J. Biochem. Physiol.* **37**, 911-917 (1959).

53. Hama, K., et al. Comprehensive quantitation using two stable isotopically labeled species and direct detection of *N*-acyl moiety of sphingomyelin. *Lipids* **52**, 789-799 (2017).

54. Ishibashi, Y., Ito, M., & Hirabayashi, Y. Regulation of glucosylceramide synthesis by Golgi-localized phosphoinositide. *Biophys. Res. Commun.* **499**, 1011-1018 (2018).

55. Yuyama, K., Sekino-Suzuki, N., Sanai, Y., & Kasahara, K. Translocation of activated heterotrimeric G protein Gao to ganglioside-enriched detergent-resistant membrane rafts in developing cerebellum. *Biol. Chem.* **282**, 26392-26400 (2007).

56. Yan, G., *et al*. Adaptive response to BET inhibition induces therapeutic vulnerability to MCL1 inhibitors in breast cancer. https://doi.org/10.1101/711895 (2020).

Declarations

Acknowledgements

This work was supported in part by a Grant-in-Aid for Scientific Research (C) (grant no. 18K06635 to Y.H.) from the Japan Society for the Promotion of Science (JSPS); and the Science Research Promotion Fund from the Japan Private School Promotion Foundation.

Author contributions

Y.H. and Y.N-S. designed the study, conducted the experiments, and wrote the manuscript. K.T. performed SARS-CoV-2 infection assays. M.Y., J.G., and J. I. established effector cells and target cells for the DSP assay. K.T., K.H., and T.T. performed the quantification of sphingolipids by LC-MS/MS. K.M. and A.Y. designed the experiments and prepared the manuscript.

Competing interests

The authors declare no competing interests.

Figures
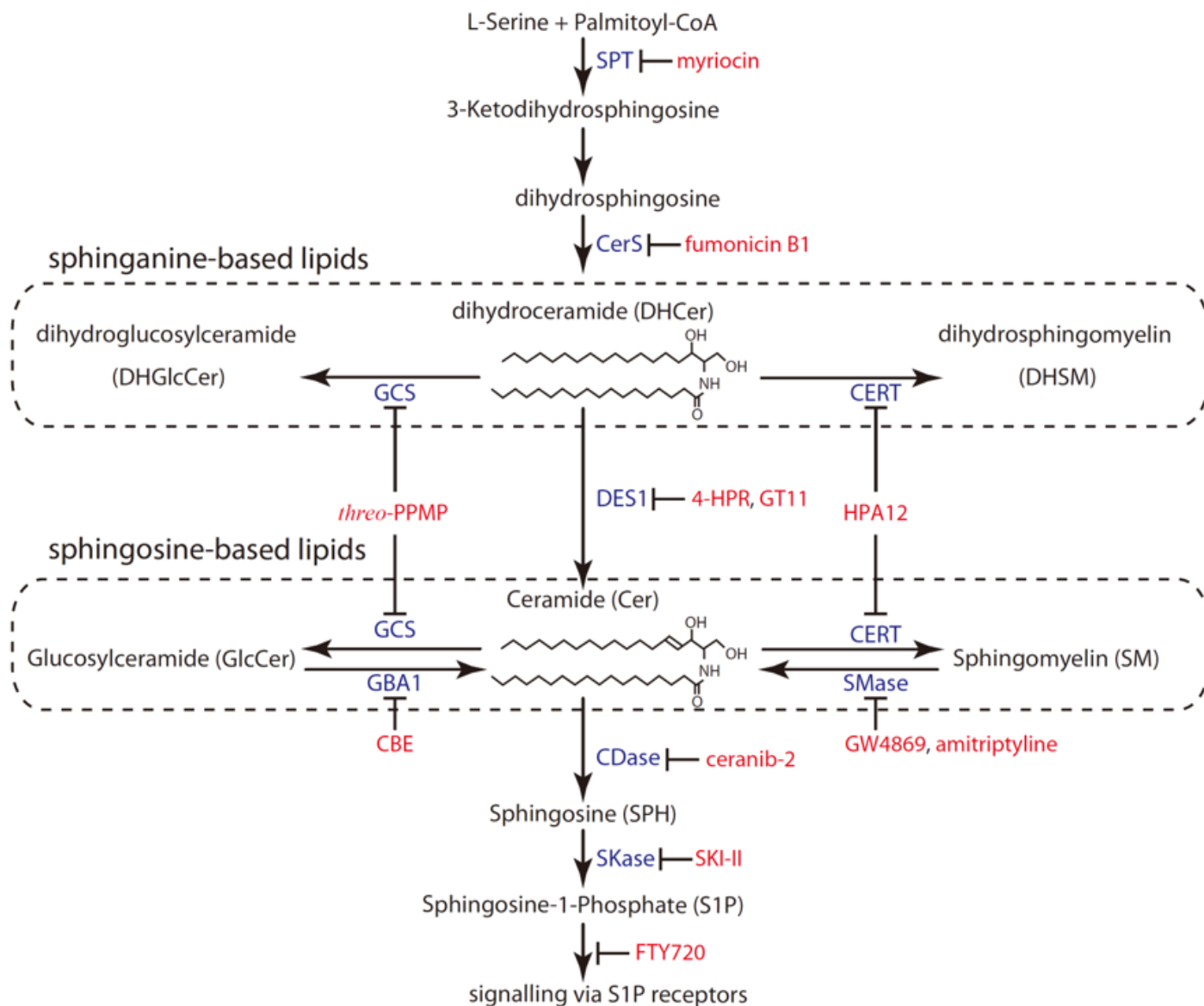
Figure 1

Enzymes involved in the sphingolipid metabolic pathway and their inhibitors in mammalian cells. The enzymes and inhibitors analysed in this study are shown in blue and red, respectively. DHCer, DHGlcCer, and DHSM are composed of a saturated sphingoid base backbone sphinganine and a fatty acid varying in length. Cer, GlcCer, and SM are composed of an unsaturated sphingoid base backbone sphingosine and a fatty acid varying in length. In mammalian cells, DHCer is desaturated by DES1, generating a 4,5-trans-double bond to form Cer. Abbreviations: CBE, conduritol B epoxide; 4-HPR, N-(4-hydroxyphenyl)retinamide; SPT, serine palmitoyltransferase; CerS, ceramide synthase; DES1, dihydroceramide Δ4-desaturase 1; GCS, glucosylceramide synthase: GBA1, β-glucocerebrosidase; CERT, ceramide transport protein; SMase, sphingomyelinases; CDase, ceramidase; and SKase, sphingosine kinase
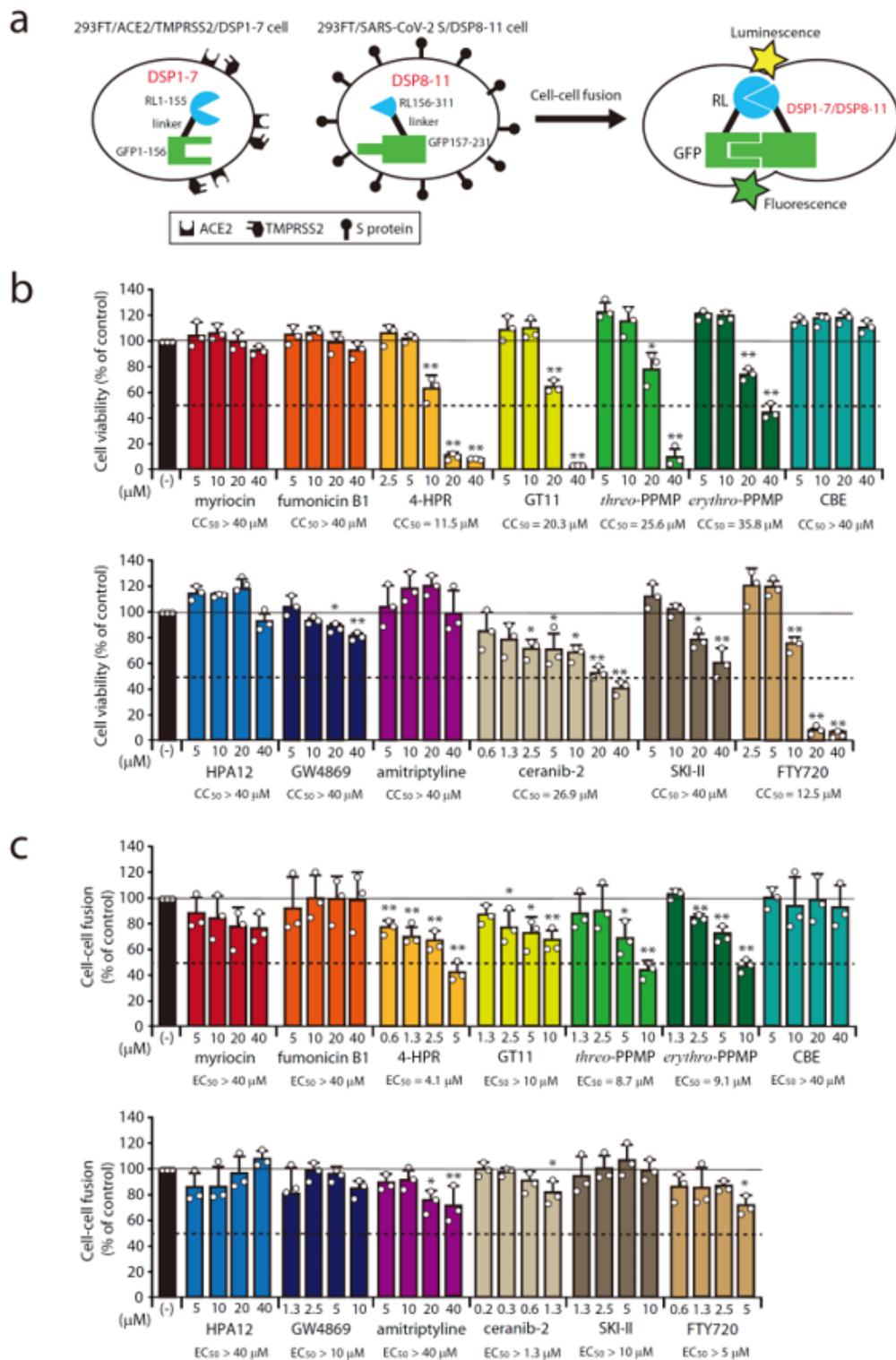
Figure 2

Effect of inhibitors of sphingolipid-metabolizing enzymes on SARS-CoV-2 S protein-mediated membrane fusion, as examined by the dual split protein (DSP) assay. The effects of compounds on cell viability and cell-cell fusion were examined in 293FT/ACE2/TMPRSS2/DSP1-7 cells treated for 2 days with the indicated concentrations of the compounds. (a) DSP-based cell-cell fusion assay is a rapid and safe assay system without infectious viruses to monitor SARS-CoV-2 S protein and its receptor angiotensin-

converting enzyme 2 (ACE2) dependent membrane fusion. DSP1-7 has the structure Renilla luciferase (RL)1-155-glycine linker-green fluorescent protein (GFP)1-156. DSP8-11 has the structure Met-RL156-311-glycine linker-GFP157-231. DSP1-7 and DSP8-11 reassociate efficiently, resulting in reconstitution of a functional RL and GFP to generate luminescent and fluorescent signals, respectively. (b) Cell viability was examined using the WST-8 assay. Results are normalised to the rate of cell viability in vehicle/ dimethyl sulfoxide (DMSO)-treated cells. (c) The susceptibility of cell-cell fusion was examined using the DSP-based cell-cell fusion assay. Results are normalised to the rate of cell-cell fusion in vehicle/DMSO-treated cells. Values represent the mean ± S.D. from three independent experiments. Statistical significance was determined by one-way ANOVA followed by Dunnett test for multiple comparisons; * $p < 0.05$, ** $p < 0.01$ when compared with vehicle/DMSO-treated cells. CC50 and EC50 values were determined using GraphPad Prism 6 software. Abbreviations: CC50, 50% cytotoxic concentration; EC50, 50% effective concentration
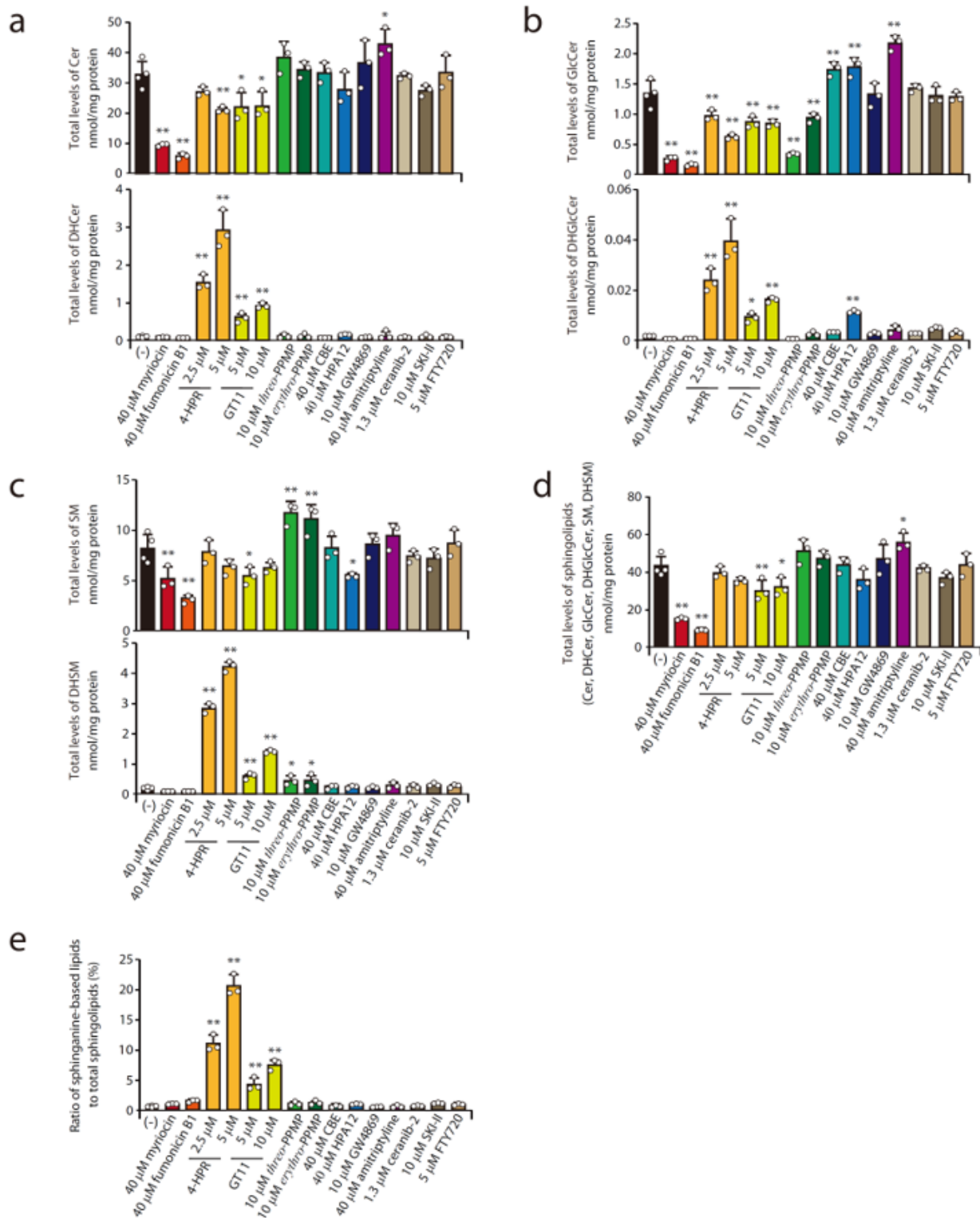
Figure 3

Effect of inhibitors of sphingolipid-metabolizing enzymes on cellular sphingolipid levels. 293FT/ACE2/TMPRSS2/DSP1-7 cells were treated for 2 days with the indicated concentrations of the compounds. The cellular sphingolipid levels of compound-treated cells were quantified by liquid chromatography with tandem mass spectrometry (LC-MS/MS) analysis. (a) Cer (upper panel) and DHCer (lower panel), (b) GlcCer (upper panel) and DHGlcCer (lower panel), (c) SM (upper panel) and DHSM

(lower panel), (d) total sphingolipids (Cer, DHCer, GlcCer, DHGlcCer, SM, and DHSM), and (e) the ratio of saturated sphinganine-based lipids (DHCer, DHGlcCer, and DHSM) to total sphingolipids. Values represent the mean ± S.D. from at least three independent experiments. Statistical significance was determined by one-way ANOVA followed by Dunnett test for multiple comparisons; * $p < 0.05$, ** $p < 0.01$ when compared with vehicle/ dimethyl sulfoxide (DMSO)-treated cells. Abbreviations: CBE, conduritol B epoxide; 4-HPR, N-(4-hydroxyphenyl)retinamide; Cer, ceramide; DHCer, dihydroceramide; GlcCer, glucosylceramide; DHGlcCer, dihydroglycosylceramide; SM, sphingomyelin; DHSM, dihydrosphingomyelin
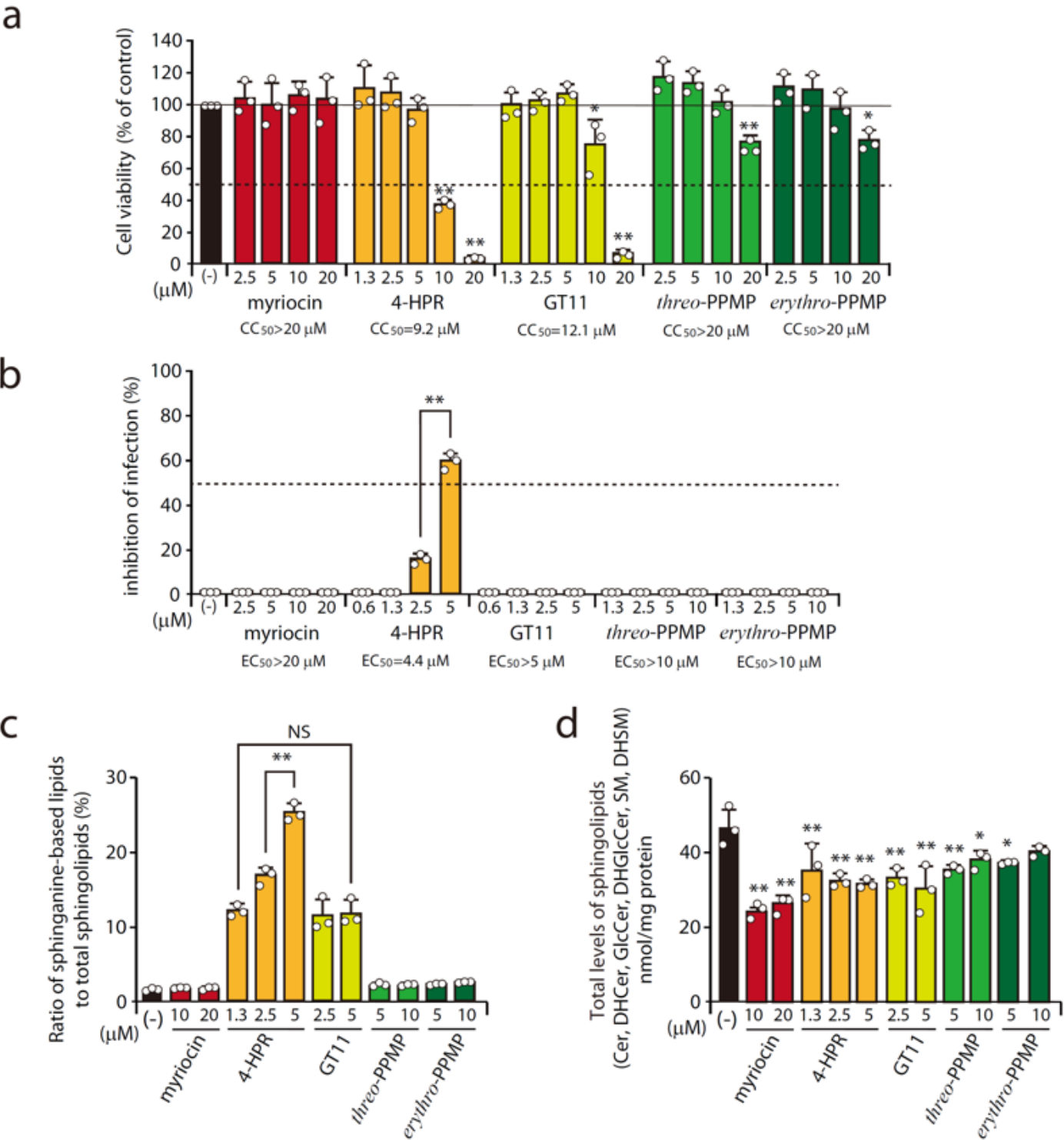
Figure 4

Effect of inhibitors of sphingolipid-metabolizing enzymes on SARS-CoV-2 infection. VeroE6TMPRSS2 cells were treated for 3 days with the indicated concentrations of compounds. (a) Cell viability was examined using the WST-8 assay. Results are normalised to the rate of cell viability in vehicle/ dimethyl sulfoxide (DMSO)-treated cells. (b) Antiviral activity was measured by reducing the SARS-CoV-2-induced cytopathic effect in VeroE6TMPRSS2 cells. Results were expressed as percentage of inhibition in compound-treated cells compared with vehicle/DMSO-treated cells. (c) Ratio of saturated sphinganine-based lipids (DHCer, DHGlcCer, and DHSM) to total sphingolipids. (d) Cellular levels of total sphingolipids (Cer, DHCer, GlcCer, DHGlcCer, SM, and DHSM). Values represent the mean ± S.D. from three independent experiments. Statistical significance was determined by one-way ANOVA followed by Dunnett test when compared with vehicle/DMSO-treated cells (a, d) and Tukey-Kramer test (b, c); $* p < 0.05$, $** p < 0.01$. Abbreviations: 4-HPR, N-(4-hydroxyphenyl)retinamide; Cer, ceramide; DHCer, dihydroceramide; GlcCer, glucosylceramide; DHGlcCer, dihydroglycosylceramide; SM, sphingomyelin; DHSM, dihydrosphingomyelin
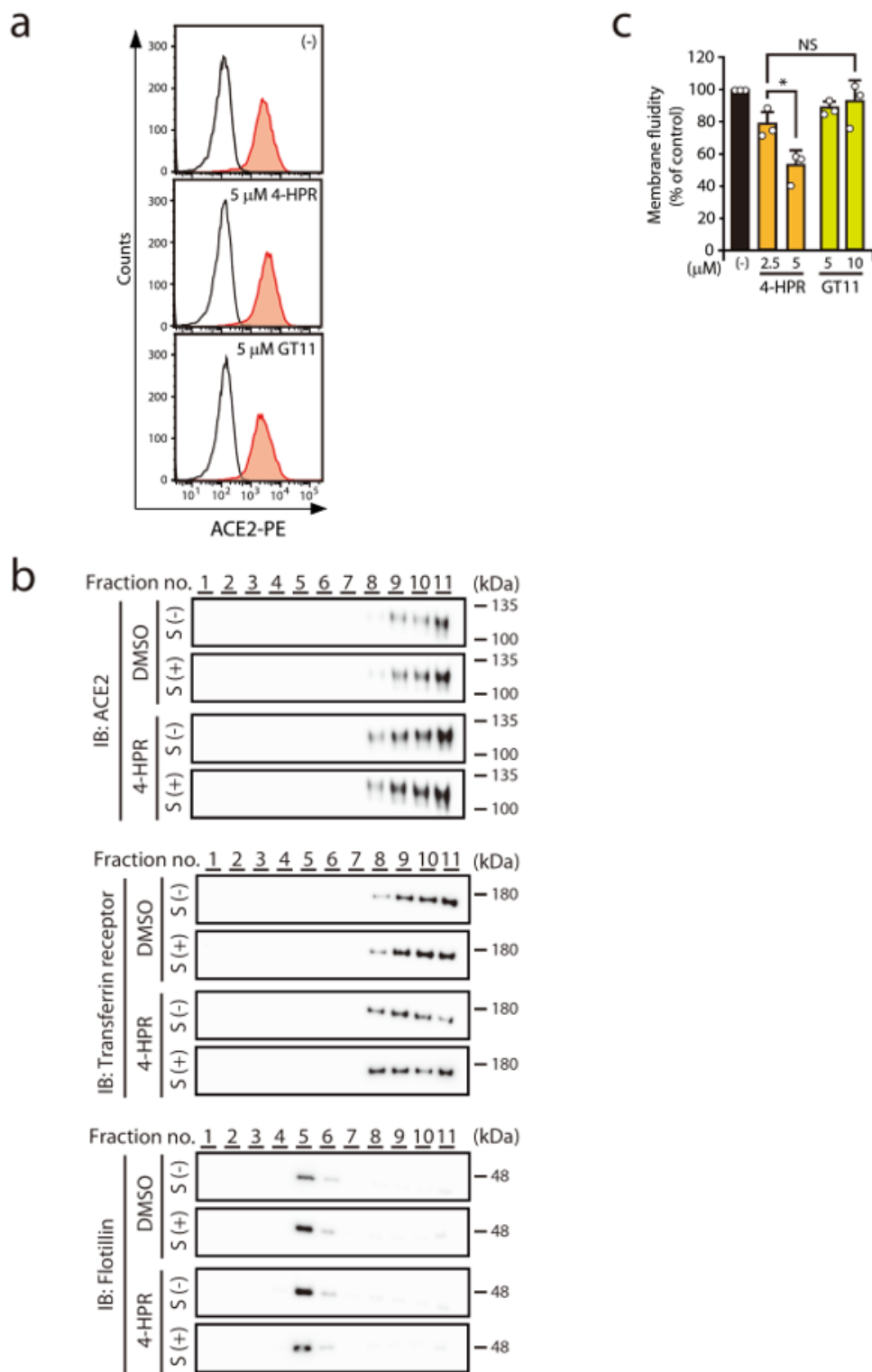
Figure 5

Effect of 4-HPR on cell-surface levels of ACE2, localization of ACE2 in membrane microdomains, and membrane fluidity. 293FT/ACE2/TMPRSS2/DSP1-7 cells were treated for 2 days with the indicated concentrations of compounds. (a) Cell-surface expression levels of ACE2 in compound-treated cells were analysed by flowcytometry using an anti-ACE2 antibody (filled histogram). Open histograms indicate the isotype control. One representative experiment is shown, and similar results were obtained in three

independent experiments. (b) Isolation of lipid rafts. Target cells were stimulated for 30 min with or without SARS-CoV-2 spike (S) protein-expressing cells, denoted by S (+) and S (-), respectively. Sucrose gradients were harvested in 1 mL fractions (fraction 1, top of the gradient; fraction 11, bottom of the gradient), and each fraction was analysed by SDS-PAGE and immunoblotted with anti-ACE2, anti-transferrin receptor (non-raft marker), or anti-flotillin (raft marker) antibodies. One representative experiment is shown, and similar results were obtained in three independent experiments. (c) Membrane fluidity in cells treated with 4-HPR or GT11 was examined with a fluorescent lipophilic pyrene probe. Results are normalised to the rate of membrane fluidity in vehicle/DMSO-treated cells. Values represent the mean ± S.D. from three independent experiments. Statistical significance was determined by one-way ANOVA followed by Tukey-Kramer test; * $p < 0.05$. Abbreviations: 4-HPR, N-(4-hydroxyphenyl)retinamide; DMSO, dimethyl sulfoxide; NS, not significant